Acta Acustica 2024, **8**, 11

https://doi.org/10.1051/aacus/2024001

Available online at:
https://acta-acustica.edpsciences.org

Technical & Applied Article

Open Access

Vibration and impact sound properties of hybrid steel-timber floor structures

Bettina Chocholaty[1,*], Nicolaas Bernardus Roozen[2,1], Karl-Alexander Hoppe[1], Marcus Maeder[1], and Steffen Marburg[1]

[1] Chair of Vibroacoustics of Vehicles and Machines, Department of Engineering Physics and Computation, TUM School of Engineering and Design, Technical University of Munich, Boltzmannstr. 15, 85748 Garching n. Munich, Germany
[2] Laboratory of Soft Matter and Biophysics, Katholieke Universiteit Leuven, Celestijnenlaan 200D, 3001 Leuven, Belgium

Received 31 October 2023, Accepted 19 January 2024

Abstract – Lightweight floor structures, such as timber or hybrid timber floors, face challenges associated with excessive vibrations and elevated levels of low-frequency impact sound. Especially here, accurate prediction of a floor's vibration and acoustic behavior is essential. However, typical laboratory testing of building elements is costly and time-consuming. To reduce costs, in this study, adapted simulations are carried out on two types of hybrid steel-timber floor structures to evaluate vibrations and impact sound. The hybrid elements are made of laminated veneer lumber as the top and bottom layers and a trapezoidal steel component as the web. Vibration measurements are used in combination with Bayesian optimization to efficiently calibrate Finite Element models, which are subsequently utilized to quantify and validate the floor structures regarding vibrations and impact sound. The two types of cross-sections, i.e., closed and open, are investigated and compared. The impact sound pressure level computations reveal promising results in predicting the behavior of the hybrid structures. However, further countermeasures are required to fulfill vibration serviceability requirements.

Keywords: Hybrid steel-timber floor, Vibrations, Impact sound, Laminated veneer lumber

1 Introduction

With the growing significance of carbon neutrality and environmental sustainability, the construction industry is actively developing sustainable solutions. Research on sustainable construction has recently expanded beyond conventional materials to encompass hybrid structures that incorporate timber in conjunction with steel [1–3], and concrete [4, 5]. These hybrid building elements have led to a range of investigations involving aspects such as vibration characteristics [1, 2], economic viability, environmental sustainability [3], and safety performance [6]. One notable area of concern in these modern hybrid structures, particularly in the context of extended spans and slender designs for lightweight floors such as wood and hybrid wood floors, evolves around their susceptibility to low resonance frequencies and annoying vibrations, which can potentially cause discomfort among occupants [7, 8]. Consequently, a significant challenge in the context of large-span timber floors lies in the exceedance of allowable vibration limits, thus making vibration serviceability a paramount criterion for design [9].

As an example, research by Hassan et al. [10] illustrates that in terms of deformations, Cross-Laminated Timber slabs with spans of 7 m and relatively modest thickness can be accommodated. However, issues arise as natural frequencies dip below 8 Hz for spans of approximately 4.5 m [10]. In such scenarios, composite or hybrid timber structures emerge as potential solutions. Perković et al. [11], for instance, determined a natural frequency of approximately 10 Hz for a hybrid concrete-timber floor with a 7-m span.

Furthermore, lightweight structures like timber or hybrid timber floors often encounter challenges with impact sound insulation [12]. Typically, building standards and regulations rely on laboratory testing for assessing the suitability of floor structures. However, these laboratory tests, especially those concerning impact sound insulation, are time-consuming and costly [13, 14] and are conducted in certified testing facilities. In the context of vibrational characteristics, either calculations or certified measurements are imperative [15]. Therefore, when adequately executed, simulations have emerged as an appealing alternative to laboratory tests.

Simulation-based engineering design often employs numerical models such as those based on the Finite Element

*Corresponding author: bettina.chocholaty@tum.de

Method (FEM), a tool extensively used by engineers across various disciplines. In practice, there tends to be a discrepancy between FEM predictions and actual test results, attributed to model form errors and approximation errors, both considered types of epistemic uncertainty [16]. To minimize the discrepancy between simulations and measurements, model parameters are iteratively adjusted, a procedure referred to as model updating. This iterative process reduces approximation errors and enhances both the reliability and accuracy of the model. The procedure involves the identification of model parameters by minimizing a problem-specific objective function [17]. Various approaches have been proposed for this purpose, whereas the approach of Bayesian optimization, in particular, offers a means to minimize the need for extensive model evaluations [18]. Its efficiency results from employing Gaussian process regression and an acquisition function for an iterative search of optimal model parameters [19].

Furthermore, recognizing the challenges presented by vibroacoustic properties of hybrid steel-timber floors, recent research [2, 20, 21] has explored innovative floor elements. In [2], the analysis focuses on a structure comprising a wooden plate combined with an H-shaped steel beam, primarily evaluating its vibration serviceability. In [20], a modular hybrid steel-timber floor constructed by Cross Laminated Timber and a U-shaped steel beam is studied experimentally. Meanwhile, [21] delves into the vibrational behavior of a hybrid steel-timber structure featuring top and bottom laminated veneer lumber (LVL) plates and a trapezoidal steel web floor element in between, with a particular emphasis on the influence of joints on overall vibroacoustics.

However, despite these valuable contributions, there remains a need for a comprehensive assessment of the acoustic properties of hybrid timber-steel structures, which are relevant for the applicability of the building elements in practice. Moreover, the structure examined in [21] has yet to be subjected to an investigation regarding its vibration serviceability. This study addresses this gap by studying both vibration serviceability and impact sound levels of the hybrid floors presented in [21]. To achieve this objective, the applied approach involves the calibration of a Finite Element model (FE model) using Bayesian optimization techniques [22]. The Bayesian optimization framework is chosen since it requires fewer model evaluations for a minimization than commonly used approaches by applying Gaussian process regression [18]. The calibration process is based on data derived from experimental vibration analysis, which allows the identification of critical parameters associated with the joints within these hybrid structures. Subsequently, using the calibrated simulation model, vibration limits and impact sound criteria are evaluated, providing valuable insights into the applicability and performance of these innovative floor elements. As a result, this research offers a comprehensive numerical exploration of the vibroacoustic behavior of a novel LVL-trapezoidal steel floor design. These findings, in turn, offer initial assessments for the prospective integration of these building components into sustainable construction practices.

2 Hybrid steel-timber floor structures

This study numerically analyzes hybrid structures composed of LVL and trapezoidal steel frames. In detail, it is constructed by top and bottom LVL plates with a trapezoidal steel core in between. The structural components are connected by fasteners whose stiffness values are unknown in advance. The numerical analysis is conducted using FEM. First, a calibration of the unknown joint parameters p is performed utilizing numerically determined natural frequencies as well as mode shapes and results from experimental modal analyses on small-scale test specimens, i.e., $S1^*$ and $S2^*$. Subsequently, the updated joint parameters $p_{n_{\mathrm{it}}}$ are used in an FE simulation to analyze large-scale floor specimens, i.e., $S1$ and $S2$, regarding vibration dose values (VDV) and impact sound pressure levels. The impact sound pressure level simulations use a numerically implemented tapping machine load. The overall workflow is visualized in Figure 1.

2.1 Description of investigated structures and simulation models

Two configurations are investigated: a closed ($S1$) and an open ($S2$) cross-section. Snippets of the test specimens are visualized in Figure 2 together with their geometric properties, which are also listed in Table 1.

According to ISO 10140-5 [23], the recommended size of a floor structure, which is to be analyzed concerning impact sound, is given as 10–20 m^2, and the shorter edge should be greater than 2.3 m. Hence, the dimensions of 3.6 m × 2.8 m are chosen for the hybrid floors (Tab. 1). However, due to the testing facility's limited spatial capacities, it has been impossible to carry out vibration measurements on the entire floor structures as given in Table 1. Hence, smaller specimens are used for the model validation and calibration, i.e., a closed $S1^*$ and an open cross-section $S2^*$.

The main difference between the open and closed cross-sections lies in the design of the lower timber plate, which is either a continuous wooden panel for closed cross-sections or made of several separate panels for open configurations. Based on preliminary structural investigations, it has been determined that the upper screw connection may be too weak in terms of load-carrying capacity and that nails would be beneficial for the upper joint. However, as the nail connection can only be made from the steel side, the open variant has been designed. The respective mounting direction of the fasteners can also be seen in Figure 2. Obviously, the different geometry, fasteners, and materials used for both types of cross-sections influence the dynamic behavior, e.g., the modal properties, of the investigated systems, which is why the two types are subsequently compared concerning VDV and impact sound insulation.

In the case of the closed form, both LVL plates are built of the material *BauBuche*[1] *Type Q* (*BB-Q*). For the open

[1] Hardwood LVL by Pollmeier Massivholz GmbH & Co.KG, D-99831 Amt Creuzburg, Germany.

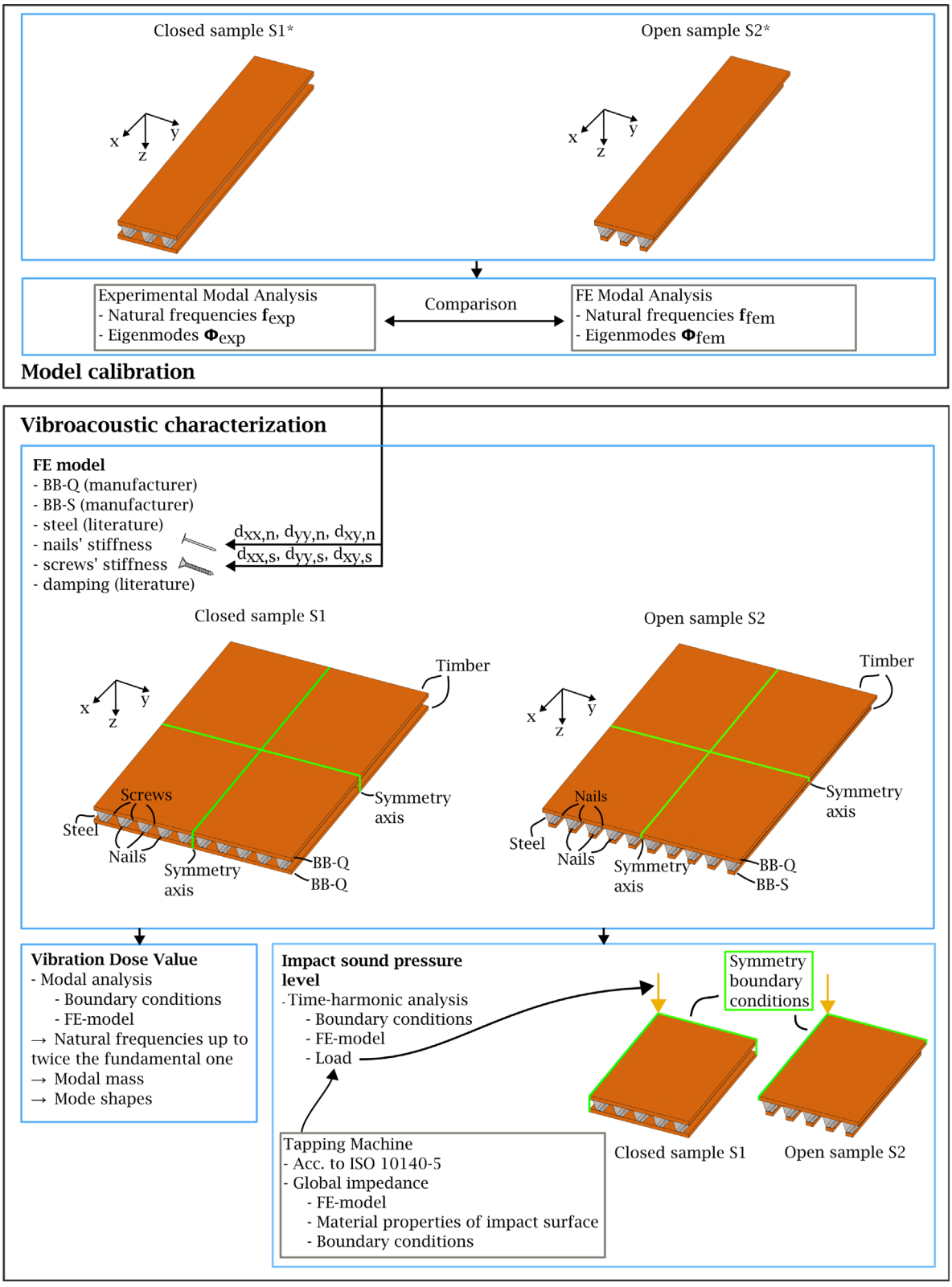

Figure 1. Overall workflow of the study: calibration of unknown model parameters p is performed utilizing numerically determined natural frequencies as well as mode shapes and results from experimental modal analyses on the small-scale test specimens, $S1^*$ and $S2^*$. The updated parameters $p_{n_{it}}$ are used in a subsequent Finite Element simulation to analyze the large-scale floor specimens, $S1$ and $S2$, regarding vibration dose values and impact sound pressure levels. The impact sound pressure level simulations use a numerically implemented tapping machine load.

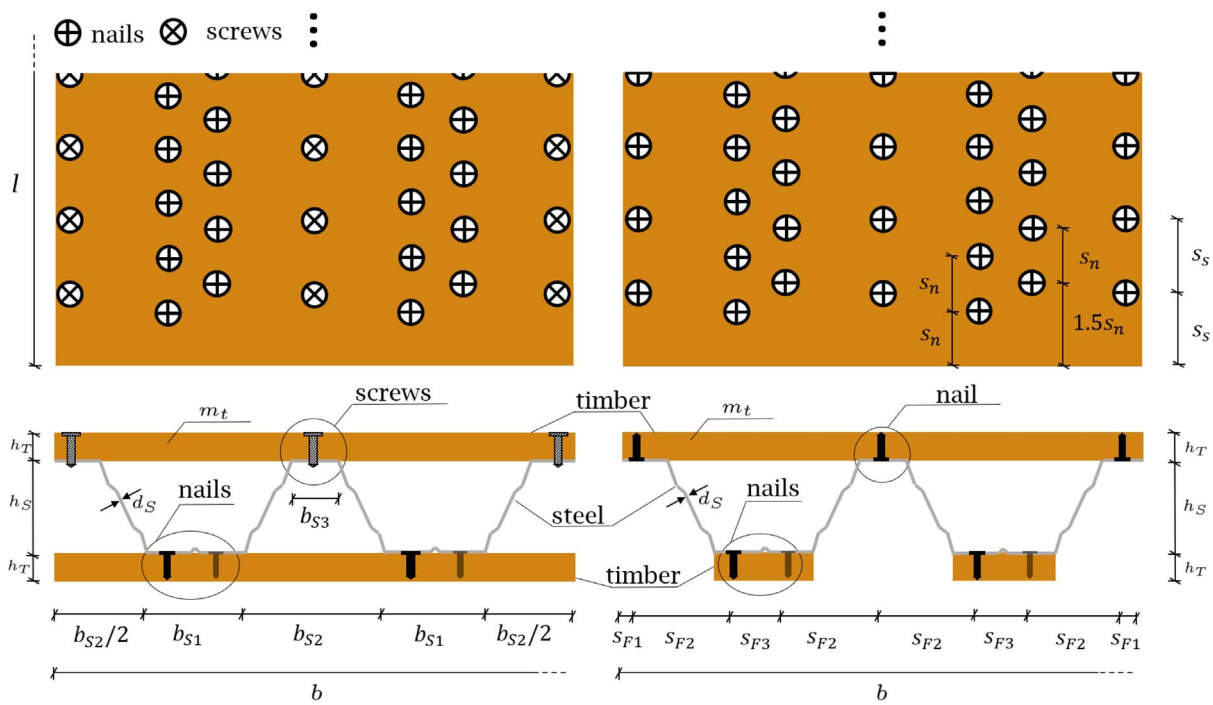

Figure 2. Snippets of closed (left, $S1$) and open (right, $S2$) hybrid LVL and trapezoidal steel elements. The lower timber plate is built of a continuous lower wooden panel for closed cross-sections and made of several separate panels for open configurations. The respective geometrical parameters are given in Table 1.

Table 1. Specimens $S1$ (closed) and $S2$ (open): the geometric parameters are defined in Figure 2. All geometric quantities are given in [m].

Sample	$S1$	$S2$
Cross-section type c_T	Closed	Open
Material of LVL plates m_T	BB-Q	BB-Q & BB-S
Length l	3.60	3.60
Width b	2.80	2.80
Thickness of LVL plates h_T	0.040	0.040
Thickness of steel plates d_S	$0.75 \cdot 10^{-3}$	$1.50 \cdot 10^{-3}$
Height of steel core h_S	0.155	0.155
Width steel b_{S1}	0.110	0.110
Width steel b_{S2}	0.170	0.170
Width steel b_{S3}	0.040	0.040
Longitudinal upper spacing s_s	0.120	0.120
Longitudinal lower spacing s_n	0.090	0.090
Transversal fastener position s_{F1}	0.010	0.010
Transversal fastener position s_{F2}	0.103	0.103
Transversal fastener position s_{F3}	0.050	0.050

Table 2. Material properties of LVL and steel provided by the manufacturer and literature [24, 25].

Material	E_x [N/m^2]	E_y [N/m^2]	G_{xy} [N/m^2]	ν_{xy} [–]	ρ [kg/m^3]
BB-Q	1.28×10^{10}	2.00×10^{9}	8.20×10^{8}	0.04	800
BB-S	1.68×10^{10}	4.70×10^{8}	7.60×10^{8}	0.04	800
Steel	2.10×10^{11}	$2.10 \times 10^{11} = E_x$	8.10×10^{10}	0.3	7850

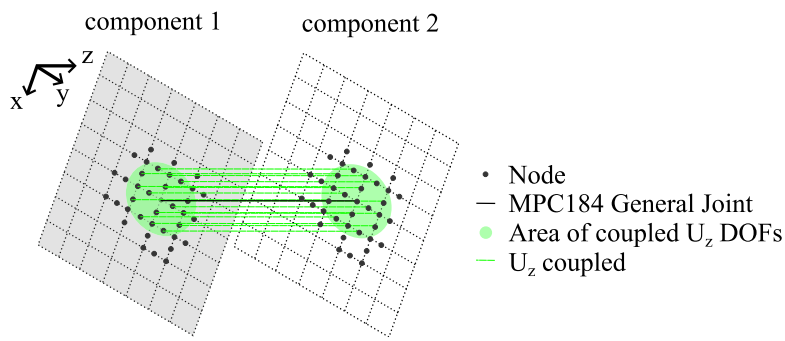

Figure 3. Fastener model: an MPC184 general joint element (represented by a black line) using a stiffness matrix between nodes related to fasteners on the substructures (grids). Coincident nodes at the interface of steel and timber are coupled related to the z-displacement (green lines) within an area surrounding the fastener (green circle).

cross-section, the upper plate is also made of *BB-Q* whereas the lower one is made of *BauBuche Type S* (*BB-S*) [24]. The respective material properties provided by the manufacturer [24] or taken from literature [25] are given in Table 2. The numerical studies use the commercial FE software *ANSYS* [26]. For the FE model, the structural components are represented by quadratic shell elements (SHELL281) with the provided orthotropic material characteristics for the timber parts and isotropic material properties for the steel sheets. Both specimen cross-section types use a trapezoidal core using steel with a nominal yield strength of $f_{y,k} = 320$ N/mm^2. However, the thickness of the steel core differs for the open, $d_S = 1.5$ mm, and closed, $d_S = 0.75$ mm, configuration. Furthermore, comparing the open and closed cross-sections, the fastener type varies due to the manufacturing process of the building elements. For the open configuration, nails[2] join the steel plates with the upper and the lower LVL plate. In the closed case, nails are only applied to join the lower LVL plate to the steel core. The upper LVL plate is attached through screws[3]. The respective positions of the fasteners are visualized in Figure 2.

For all fasteners, the ANSYS element type "MPC184 general joint" is utilized. These elements allow specifying a stiffness matrix with 21 entries:

$$d_{\text{joint}} = \begin{bmatrix} d_{11} & d_{12} & d_{13} & d_{14} & d_{15} & d_{16} \\ & d_{22} & d_{23} & d_{24} & d_{25} & d_{26} \\ & & d_{33} & d_{34} & d_{35} & d_{36} \\ & & & d_{44} & d_{45} & d_{46} \\ & & sym. & & d_{55} & d_{56} \\ & & & & & d_{66} \end{bmatrix}. \quad (1)$$

Here, the indices "1", "2", and "3" denote displacements in the x-, y-, and z-direction, respectively. Moreover, the indices "4", "5", and "6" refer to rotational degrees of freedom (DOFs) around the x-, y- and z-axis, respectively. The coordinate directions are visualized in Figure 1. A preliminary analysis conducted as part of this work revealed only three stiffness parameters, i.e., $d_{11} = \mathrm{d}_{xx}$, $d_{22} = d_{yy}$, and $d_{12} = d_{xy}$, that significantly influence the vibrational behavior of the structure. Hence, all other entries of the fasteners' stiffness matrix are set to zero.

The concept for the fastener model is depicted in Figure 3. In addition to the general joint elements, coupling constraints for the displacement in the z-direction are applied to closely located nodes at the interface of steel and timber surrounding the joints. The surrounding of the joints means within a radius of 0.022 m. This radius is determined through an empirical evaluation of the parameter space and leads to the best match of simulation and experimental results with the fixed value. In this surrounding area, nodes that are coincident within a certain tolerance behave as infinitely stiff coupled related to the displacement in z-direction. The tolerance is set just large enough to cover the distance between steel and timber components. This way, pairs of steel and timber component nodes are coupled concerning their displacement in z-direction.

Since the open cross-sections only use nails, denoted by the index "n", the same joint stiffness parameters are assumed for the upper (u) and lower (l) joints $d_{ij,l} = d_{ij,u} = d_{ij,n}$. For the case of closed configurations, different joint parameters for upper and lower connections are set, i.e., $d_{ij,u} = d_{ij,s}$ and $d_{ij,l} = d_{ij,n}$, where the index "s" refers to properties related to screws. As the fastener models' parameters are initially unknown, they constitute the unknown model parameters p, identified using model calibration and vibration measurements in the first analysis step.

The FE model uses a mesh size of $l_{\text{ele},t} \approx 0.015$ m for the timber components and of $l_{\text{ele},s} \approx 0.013$ m for the steel core. In [27], six to eight quadratic elements per wavelength have led to an acceptable error in eigenfrequencies compared to a converged solution. Hence, the bending wavelengths λ [28] are computed using the respective material properties of Table 2. The comparison of the sixth of the timber's bending wavelength $\lambda/6$ with the mesh size shows that the finite element size of the timber components is valid up to 10000 Hz, which is sufficient for the current studies. In the case of the steel parts, the used mesh size accounts for six to eight quadratic elements per wavelength in the low-frequency range. However, the mesh size is only valid up to 1300 Hz, for $S1$ with a steel thickness of $d_S = 0.75$ mm, and up to 2400 Hz, for $S2$ with a steel thickness

[2] Unpublished prototype.
[3] Thin sheet metal screws 6.0 × 90 by Reisser-Schraubentechnik GmbH, D-74653 Ingelfingen-Criesbach, Germany.

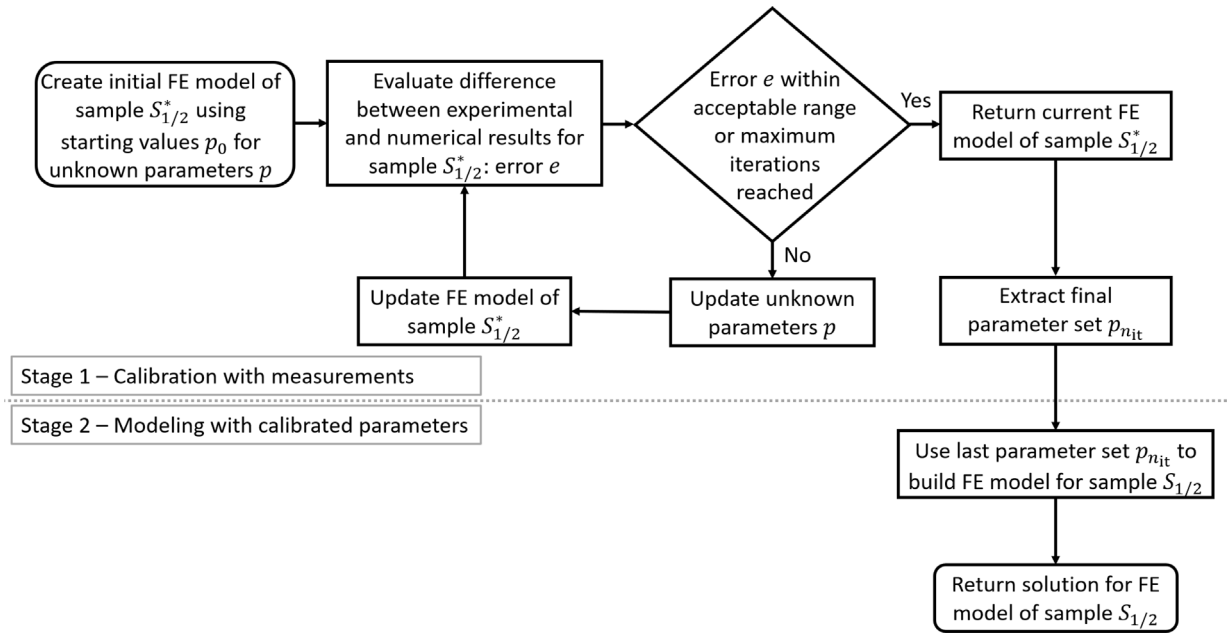

Figure 4. Flowchart of the model calibration: An FE model of the respective measured sample $S1^*$ or $S2^*$ is calibrated by iteratively adapting the unknown parameters p and computing an error e using the numerical and experimental results.

of $d_S = 1.5$ mm. Due to the limited computational resources, it becomes impossible to reduce the mesh size further. The current model for the vibroacoustic evaluation already uses approximately 0.9 million DOFs. Hence, the simulations are performed until the specified maximum frequency for the respective cases.

2.2 Model calibration

For the model calibration, the closed and open samples $S1^*$ and $S2^*$ are used. The in-plane dimensions of the test specimens are changed to 3.50 m x 0.84 m due to the limited spatial capacities of the testing facilities. All other properties remain as specified for the large-scale samples in Table 1.

2.2.1 Numerical approach

The FE model of the respective sample $S1^*$ or $S2^*$ is calibrated by iteratively adapting the model parameters p, i.e., the joint stiffnesses values of the nails $d_{ij,n}$ and the screws $d_{ij,s}$, and computing an error e using the numerical and experimental results. An overview of the model calibration workflow is visualized in Figure 4.

Six parameters in the FE model calibration are unknown at the beginning:

$$p = [d_{11,s}, d_{12,s}, d_{22,s}, d_{11,n}, d_{12,n}, d_{22,n}]. \quad (2)$$

The closed specimen uses all six of them, whereas the open specimen utilizes only the three parameters related to nails, i.e., $d_{ij,n}$. First, the calibration of the nails' parameters is conducted using the data of the open specimen. Subsequently, those resulting nail parameters are used in the model of the closed specimen. Second, the screws' parameters are calibrated utilizing the model and the measurement data of the closed specimen.

The free boundary conditions and the load position are adopted in the model in correspondence with measurement setups. Furthermore, a frequency resolution of $\Delta f = 1.0$ Hz is applied in the frequency range of interest $f_{\text{low}} \in [10, 312.5]$ Hz, which covers the measured frequency range.

2.2.2 Experimental approach

Vibration measurements are performed on the two test samples $S1^*$ and $S2^*$ to identify modal properties through experimental modal analysis [29]. Therefore, a pseudo-random excitation is applied to the specimens by means of a B&K[4] modal exciter type 4284 connected to the test samples utilizing a stinger at one point on the specimen. Heavy-duty slings are used to suspend the test samples in the measurement setup (Fig. 5) to simulate free boundary conditions in the FE model.

A force transducer (B&K Force Transducer Deltatron Type 8230) measures the force applied to the specimens. Moreover, a scanning Laser Doppler Vibrometer PSV-500[5] (LDV) records the surface velocity on the specimen's side opposite the force application position on a distributed grid of scan points. The measured force and velocity data are combined to compute the frequency response function. A Fast Fourier Transformation transforms the recorded time data to the frequency domain. The resulting spectra are averaged over 25 measurements for each scan point in the complex plane. Furthermore, the signals are adapted using a rectangular window. The sampling rate

[4] Hottinger Brüel & Kjær GmbH, D-64293 Darmstadt, Germany.
[5] Polytec GmbH, D-76337 Waldbronn, Germany.

Figure 5. Scan setup using heavy-duty slings for suspension with Laser Doppler Vibrometer (LDV) (a) and shaker (b).

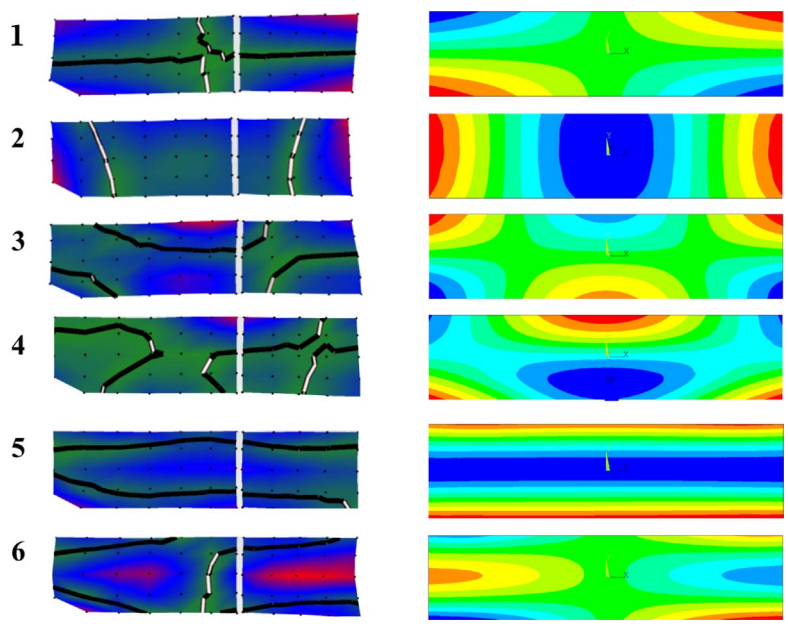

Figure 6. Mode shapes for the sample $S1^*$: experimentally determined (left) and numerically simulated (right) after model calibration.

$f_{\text{smp}} \approx 781$ Hz and the frequency resolution of $\Delta f \approx 390$ mHz are applied. All data acquisition tasks utilize the Polytec software. Further details on the measurements are given in [21].

After performing experimental modal analyses, the experimentally determined modes visualized in Figure 6 for the closed specimen $S1^*$ and in Figure 7 for the open specimen $S2^*$ are used to calibrate the model.

2.2.3 Parameter optimization

The respective stiffness values of fasteners are calibrated using experimental modal analysis data and the FE modal analysis results of the samples $S1^*$ and $S2^*$. A multi-objective model updating [30] is used, which considers a frequency error e_1 and a mode shape error e_2:

$$\min e(p) = \min(e_1(p) \& e_2(p)), \tag{3}$$

$$e_1(p) = \sum_{m=1}^{N_m} (e_{r,m})^2 = \sum_{m=1}^{N_m} \left(\left| \frac{f_{\text{exp},m} - f_{\text{fem},m}}{f_{\text{exp},m}} \right| \right)^2, \tag{4}$$

$$e_2(p) = \sum_{m=1}^{N_m} \left(\frac{1 - \text{MAC}_m}{\text{MAC}_m} \right)^2, \tag{5}$$

where f_{exp} and f_{fem} are the experimentally and numerically determined natural frequencies, respectively, and MAC_m is the modal assurance criterion of the mode shapes computed, as described in [31]:

$$\text{MAC}_m = \frac{(\Phi_{\text{exp},m} \Phi_{\text{fem},m})^2}{(\Phi_{\text{exp},m}^T \Phi_{\text{exp},m})(\Phi_{\text{fem},m}^T \Phi_{\text{fem},m})}. \tag{6}$$

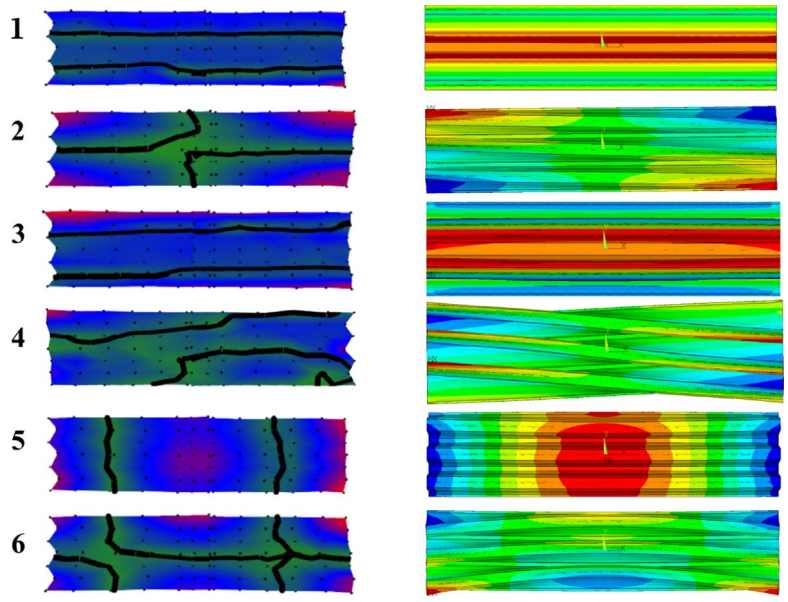

Figure 7. Mode shapes for the sample $S2^*$: experimentally determined (left) and numerically simulated (right) after model calibration.

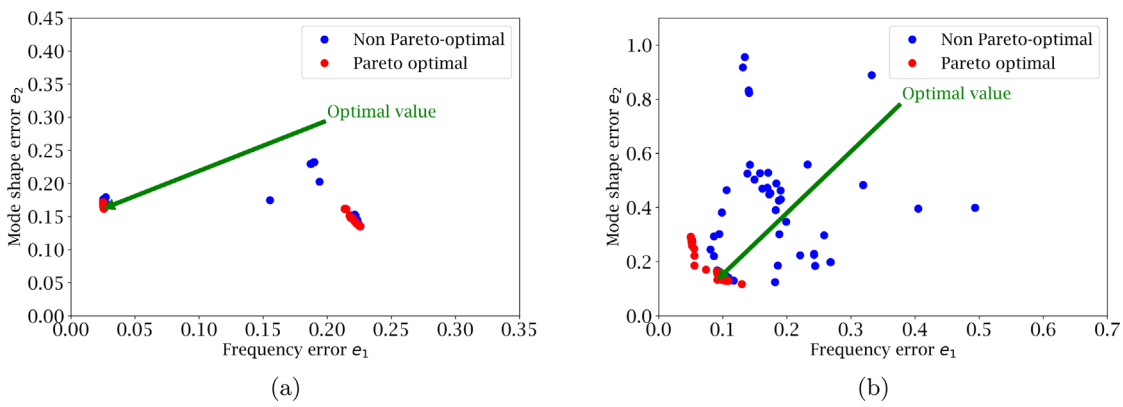

Figure 8. Pareto optimal front of the multi-objective optimization for the closed $S1^*$ (a) and open $S2^*$ (b) specimen.

Here, N_m equals the number of eigenfrequencies and modes considered in the optimization and is assigned as $N_m = 6$ as six modes per specimen, i.e., $S1^*$ and $S2^*$, are taken into account. A multi-objective optimization is chosen instead of a single-objective optimization to circumvent the choice of weightings of the errors e_1 and e_2. The optimization goal is to identify the best solution in the Pareto optimal front [32]. Hence, based on the evaluations of the objective functions of equations (4) and (5), the Pareto optimal front, $e = (e_1(p), e_2(p))$, is computed. For conflicting objectives, a singular optimal solution does not exist. Instead, there is a collection of alternative solutions referred to as Pareto optimal solutions. These solutions are optimal because no other solutions within the parameter space surpass them when considering all objectives [33]. Thus, a criterion is established to determine the most suitable solution at the Pareto optimal front by summing both errors for each point on the Pareto optimal front (Fig. 8) and taking the set of parameters, which leads to the smallest sum of errors as the best solution:

$$e = \min(\mathbf{e}_1(p) + \mathbf{e}_2(p)). \tag{7}$$

As an optimization method, Bayesian Optimization is utilized due to its benefits explained hereafter. First, regarding the number of function evaluations needed, Bayesian optimization is a highly efficient method. Furthermore, it performs well even when the objective function contains multiple local maxima. The method can integrate prior beliefs concerning the problem, which aids in guiding the sampling process and balancing the exploration and exploitation of the search space. As it relies on Bayes' theorem, the prior knowledge embodies our initial beliefs concerning the range of potential objective functions. Despite the unknown nature of the cost function, it is justifiable to assume that there is prior knowledge about specific properties, such as smoothness, which renders certain objective

Table 3. Numerically f_{fem} and experimentally f_{exp} determined natural frequencies [Hz], relative frequency error $e_{r,m} = |(f_{\text{exp},S1/2^*,m} - f_{\text{fem},S1/2^*,m})/f_{\text{exp},S1/2^*,m}|$ and MAC before and after the automatic model calibration: $m \in [1, 6]$ for $S1^*$ and $S2^*$.

$S1^*$		Before			After		
m	$f_{\text{exp,m}}$	$f_{\text{fem},m}$	$e_{r,m}$	MAC_m	$f_{\text{fem},m}$	$e_{r,m}$	MAC_m
1	48.3	54.3	0.12	0.98	50.8	0.05	0.98
2	76.6	81.3	0.06	0.81	71.6	0.07	0.84
3	78.7	95.8	0.22	0.77	88.0	0.12	0.74
4	90.4	90.0	0.00	0.51	90.3	0.00	0.77
5	102.1	100.7	0.01	0.81	100.5	0.02	0.80
6	114.5	136.7	0.19	0.78	106.9	0.07	0.67
$S2^*$		Before			After		
m	$f_{\text{exp,m}}$	$f_{\text{fem},m}$	$e_{r,m}$	MAC_m	$f_{\text{fem},m}$	$e_{r,m}$	MAC_m
1	40.0	42.7	0.07	0.90	42.7	0.07	0.90
2	49.0	51.3	0.05	0.98	49.6	0.01	0.98
3	68.1	80.2	0.18	0.92	80.1	0.18	0.92
4	77.1	96.6	0.25	0.61	94.3	0.22	0.61
5	86.9	88.6	0.02	0.97	85.1	0.02	0.97
6	105.1	100.6	0.04	0.95	97.3	0.07	0.95

functions more credible than others. As observations are accumulated, the prior distribution and the likelihood function are merged, leading to updated beliefs in the posterior distribution. For efficient sampling, Bayesian optimization employs an acquisition function to find appropriate sampling locations. This decision inherently involves a trade-off between exploration (in areas where the objective function is highly uncertain) and exploitation (sampling values where the objective function is anticipated to be high) [34]. Due to its goal to minimize the number of objective function evaluations and, thus, to reduce the computational effort, Bayesian Optimization is applied in this study.

Since the parameters for the fasteners are initially unknown, a manual search is performed first by picking and testing reasonable values. Using the best choice for the joints' stiffness values $d_{ij,s}$ and $d_{ij,n}$ of the manual search, an already acceptable match is achieved, as is visible in the columns denoted by "before" in Table 3. The label "before" is assigned since these results are computed utilizing manually found parameter values. The label "after" refers to results calculated with the parameters found by the Bayesian optimization.

The initial joints' parameters, as identified by the manual search, are given in Table 4 denoted by p_0. The properties $p_{n_{\text{it}}}$ in Table 4 refer to the values found by the automatic model calibration performed using Bayesian optimization.

The optimization, i.e., the automatic model calibration, utilizes the manually found parameters as guiding values for the bounds specified in the calibration procedure. Narrow, i.e., $\pm 25\%$ p_0, and broader, i.e., $-90\%/+1000\%$ p_0, bounds are applied to thoroughly search the parameter space. Subsequently, the pairs of errors at the Pareto front are found, and the pair of those data points with the least sum, i.e., $e = \min(\mathbf{e}_1(p) + \mathbf{e}_2(p))$ is chosen as the best

Table 4. Initial p_0 and calibrated $p_{n_{\text{it}}}$ parameters for the closed $S1^*$ and open $S2^*$ specimen: u and l denote the upper and lower joint, respectively. All values in the table refer to the properties of nails except for the entries marked by †, which refers to screw parameters.

	$S1^*$		$S2^*$	
	p_0	$p_{n_{\text{it}}}$	p_0	$p_{n_{\text{it}}}$
$d_{11,u}$	2.5e7†	9.6e6†	2.5e7	5.0e7
$d_{12,u}$	5.0e7†	9.2e5†	5.0e7	1.0e5
$d_{22,u}$	2.5e6†	1.5e8†	2.5e6	5.0e7
$d_{11,l}$	5.0e7	5.0e7	2.5e7	5.0e7
$d_{12,l}$	1.0e5	1.0e5	5.0e7	1.0e5
$d_{22,l}$	5.0e7	5.0e7	2.5e6	5.0e7

solution. The respective results of the parameter search are visualized in Figure 8, together with the Pareto optimal front for both specimens.

From the optimization computations, the parameters labeled as $p_{n_{\text{it}}}$ in Table 4 and, thus, the natural frequencies and MAC values denoted by "after" of Table 3 result.

Figure 8 shows that two groups of error combinations are formed for the test specimen $S1^*$, while there is only one for $S2^*$. For $S1^*$, one group of model solutions results in a smaller frequency error with almost equal mode error compared to the other group. Hence, a better solution is found for the group with the smaller frequency error. This aspect can also be observed in Table 3. The relative frequency error before the automatic model calibration lies above 10% for modes 1, 3, and 6, which is strongly reduced to errors below 10%, i.e., $e_{r,m} \in [0.02, 0.07]$, for all modes except the third, where it lies slightly above, i.e., $e_{r,3} = 0.12$. This improvement in frequency error comes with the price of reduced MAC values for modes 3, 5, and 6, i.e., $\text{MAC}_m \in [0.74, 0.80]$. However, the relative reduction of MAC values before and after the automatic updating lies below 0.03 for modes 3 and 5 and is only exceeded for mode 6 with a MAC value reduction of 0.08. Generally, the MAC values for specimen $S1^*$ are not as good as for the open specimen $S2^*$. Only the MAC for the first mode lies above 0.90. For modes 2 and 5, the MAC values are still above 0.80, but the values are even lower for modes 3, 4, and 6. The reason for this behavior is presumably the shape of the modes. As visualized in Figure 6, only mode 1 shows a nice and clear behavior. Modes 2–6 are either challenging to identify, non-symmetric, or both. This circumstance could stem from manufacturing inaccuracies, e.g., slight relative rotations of the components, which lead to a non-symmetric built-up, pre-stress, and pre-deformation. Furthermore, sample $S1^*$ uses a steel sheet of thickness $d_s = 0.75$ mm as opposed to $d_s = 1.5$ mm for $S2^*$, leading to individual parts of the steel frame vibrating locally, which influences the global structural behavior. Moreover, the modes are challenging to identify in the experiments, e.g., due to closely spaced modes. Consequently, due to the overall improved agreement between numerical and experimental results, the updated parameters $p_{n_{\text{it}}}$ are deemed acceptable.

For $S2^*$, in Figure 8b, only one group of model solutions exists, and the Pareto front is discernible. The Pareto criterion assesses whether a state improves by changing one target value without deteriorating another. The Pareto front shows the values that represent the best compromise. Here, no solution with a smaller frequency error could be found without causing an increase in the mode error. Due to this behavior, only a slight improvement of frequency and mode error is achieved for $S2^*$ as can be seen in Table 3: only the natural frequencies $f_{S2^*,2}$ and $f_{S2^*,4}$ become slightly closer to the experimentally determined natural frequencies. However, simultaneously, the match for $f_{S2^*,6}$ becomes slightly worse, and the MAC values do not increase. In particular, the fourth mode, which appears to be less clear than the others (Fig. 7), shows some discrepancy with the simulation results regarding natural frequency. This mode also shows a MAC of only 0.61, presumably due to the complexity of the mode shape. Moreover, the natural frequencies of the first and third modes, i.e., the bending modes in the lateral (y-) direction, are somewhat apart from the numerical results. However, a better match is challenging to obtain since, for an advantageous adaptation of the joint parameters, the other natural frequencies deviate more from their experimental counterparts. Still, all MAC values lie above 0.90 except for mode 4 due to a complex mode shape. Furthermore, except for the second lateral bending mode 3 and the unclear mode 4, the relative frequency error lies below 10%, which is satisfying. Hence, also for the open cross-section, the calibrated parameters $p_{n_{it}}$ are assumed to be suitable for the simulations related to the vibroacoustic validation, which is described in the following section.

The updated values of the fasteners are calibrated for natural frequencies up to approximately 115 Hz and are thus adaptable for the VDV calculations, which consider modes around and below this frequency. However, it should be noted that frequencies of up to 1.3 kHz and 2.4 kHz are examined in the context of impact sound tests. Therefore, uncertainty is added to the model by assuming that the joint stiffnesses from the updating procedure are suitable for these impact sound computations.

2.3 Model for vibroacoustic validation

FE analyses are performed to validate the vibration serviceability and impact sound characteristics of the hybrid steel-timber structures, as measurements are often time-consuming and costly [13, 14]. Here, the floor structures $S1$ and $S2$ (Tab. 1) without additional components, such as floating floors or walls located on the edges of the floors, are considered in the simulations. Even though these assumptions result in discrepancies between the predicted and presumably observed behavior of in-situ floors, the FE models are assumed to provide a first estimate of the applicability of the proposed hybrid floors.

The parameters $p_{n_{it}}$ (Tab. 4), i.e., the joint parameters identified by calibration, are utilized for these FE models. Given the profound influence of boundary conditions on structural vibration and sound radiation in the low-frequency regime, and in light of the unavailability of measurements for samples $S1$ and $S2$ in a built-in configuration, the investigations focus on the two extreme scenarios regarding boundary conditions: namely, clamped ("c") and free ("f"). In the clamped configuration, all degrees of freedom are constrained along the outer edges of the floor structure, whereas in the free boundary condition scenario, none are restrained. Furthermore, to increase computational efficiency and manage system matrices with respect to memory resources and disk space, symmetry boundary conditions are employed in the FE model. This approach involves discretizing and solving only one-quarter of the floor element, assuming that the remaining three-quarters can be derived through symmetry principles. The respective boundary conditions are applied along the cutting planes of the quartered floor structure. The load for impact sound computations is located in the center of the structure, which is the point of symmetry in x- and y-directions (see Fig. 1 for the definition of the coordinate system). This excitation force only excites symmetric modes in both the x- and y-directions. Therefore, applying only symmetric boundary conditions is theoretically sufficient, and no additional antisymmetric boundaries need to be considered in the response analysis.

As the VDV calculation is based on the load case of a person crossing the floor, all kinds of modes are excited and thus need to be considered. Therefore, for the computation of the VDV, symmetric, antisymmetric, and all possible combinations of support conditions are applied in the simulation to incorporate both antisymmetric and symmetric mode shapes.

The implementation of the antisymmetric and symmetric boundary conditions is performed by imposing constraints on nodes, respectively DOFs, in the planes of symmetry or antisymmetry. Hence, the following DOFs are constrained:

- For symmetry conditions
  - In the plane with the normal in x-direction: displacements in x-direction, rotations around the y-axis, rotations around the z-axis.
  - In the plane with the normal in y-direction: displacements in y-direction, rotations around the x-axis, rotations around the z-axis.
- For antisymmetric conditions
  - In the plane with the normal in x-direction: displacements in y- and z-direction, rotations around the x-axis.
  - In the plane with the normal in y-direction: displacements in x- and z-direction, rotations around the y-axis.

Furthermore, the global impedance for the impact load computation taken from the respective FE model is scaled due to symmetry considerations [35].

In contrast, the "c" and "f" boundary conditions are implemented along the outer edges as previously described. Hence, four cases are investigated:

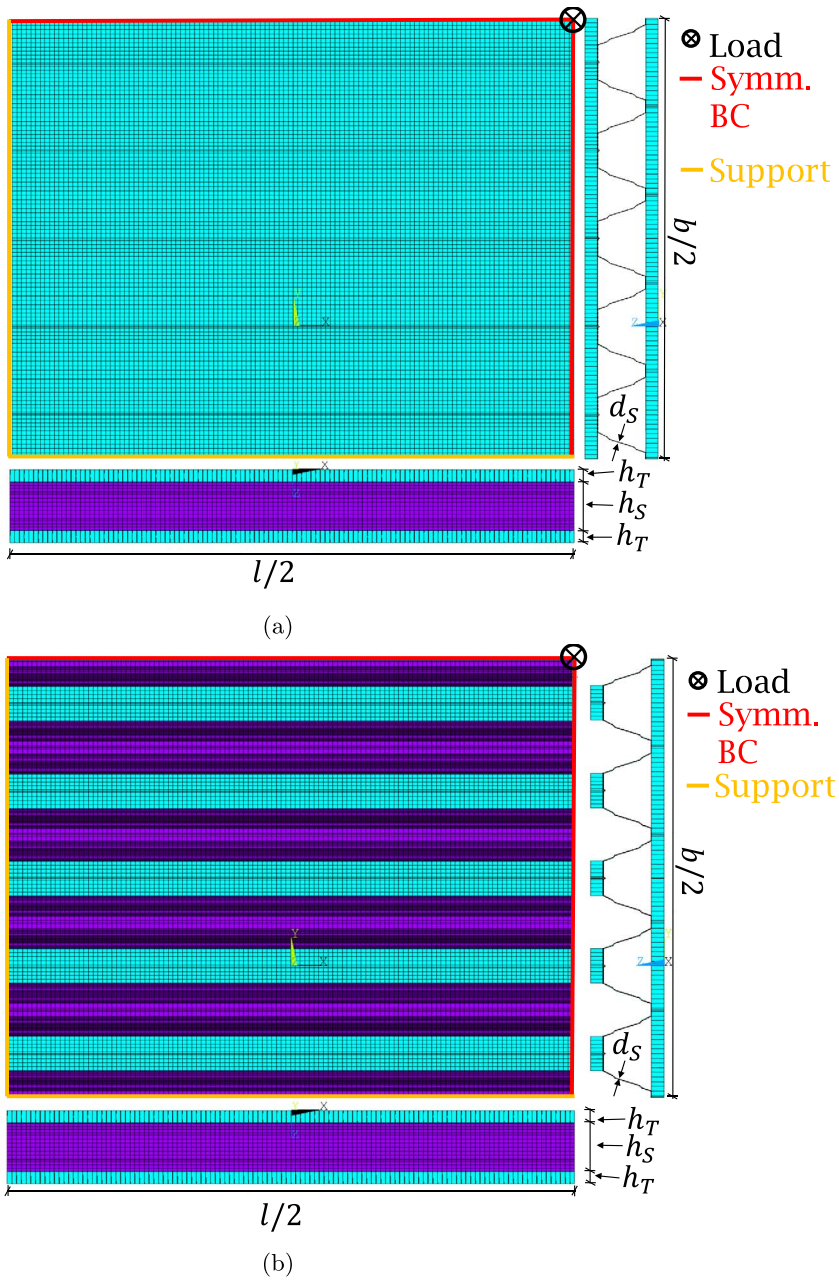

Figure 9. FE model of closed sample $S1$ (a) and open sample $S2$ (b): bottom view and side views. Steel is colored purple, and timber parts are cyan. The element thickness is visually scaled to represent the thickness of the respective component.

- Closed cross-section, clamped boundary condition: $S1,c$;
- Closed cross-section, free boundary condition: $S1,f$;
- Open cross-section, clamped boundary condition: $S2,c$;
- Open cross-section, free boundary condition: $S2,f$.

The FE models of the analyzed one-quarter of the floor structures are visualized in Figure 9.

A structural modal damping ratio of 1% is chosen according to the recommendation of the European timber standard [36]. The damping identified for the test specimens $S1^*$ and $S2^*$ is deemed inappropriate for the FE-model of the floor structures, i.e., $S1$ and $S2$, since boundary conditions significantly influence the damping of a structure [37] as well as the overall built-up. Furthermore, no structural vibration tests have been possible on large-scale floor structures in a built-in situation. The chosen damping ratio is applied as a structural loss factor $\eta_s = 0.01 \times 2$ in the FE-model for the whole analyzed frequency ranges $f_{\text{impact},S1} \in [10, 1300]$ Hz and $f_{\text{impact},S2} \in [10, 2400]$ Hz. Here, uncertainty is introduced in the simulation model since the damping value proposed by Eurocode 5 [36] applies to low frequencies related to vibrations. A timber joist floor investigated by Wang et al. [38] showed an approximate structural loss factor of 0.02 up to 2500 Hz. Although

Algorithm 3.1. Impulsive response calculation procedure

1: Compute modes and eigenfrequencies f_m up to twice the fundamental frequency f_1
2: Calculate effective footfall impulse $I_{\text{eff},m} = 54 \cdot \frac{f_w^{1.43}}{f_m^{1.30}}$ with the maximum walking frequency $f_w = 1.8$ Hz and the considered eigenfrequencies f_m
3: Compute peak velocity in each mode m: $\hat{v}_m = \Phi_{e,m}\Phi_{r,m}I_{\text{eff},m}/\hat{m}_m$ with $\Phi_{e,m}$ the value of the mode shape m at the excitation position, $\Phi_{r,m}$ the value of the mode shape m at the receiving position, $\hat{m}_m$ the modal mass of mode m
4: From this, calculate the velocity response in each mode over the period of one footfall T with ζ as the modal damping ratio: $v_m(t) = \hat{v}_m \exp(-2\pi f_m \zeta t)\sin(2\pi f_m t)$ with the modal velocity magnitude $\hat{v}_m$
5: Compute total response to each footfall $v(t) = \sum_{m=1}^{N} v_m(t) \cdot w_m$ with a weighting w_m taken from [42] as suggested in [41]
6: For a time-harmonic analysis, the total response to each football can be converted to accelerations by computing the acceleration magnitude from the velocity magnitude as $\hat{a} = (-i\omega)\hat{v}$
7: From the resulting acceleration time history, root-mean-square (RMS) response evaluated over one footfall $a_{\text{RMS}} = \sqrt{\frac{1}{T}\int_0^T a(t)^2 \text{dt}}$

this work deals with a pure timber instead of a hybrid steel-timber floor, the chosen loss factor of 0.02 is deemed acceptable as a first estimate, as currently, no investigations exist on the impact sound behavior of hybrid steel-timber floors such as the presently studied ones.

3 Vibroacoustic criteria

The updated and adapted FE model is used in the following sections to evaluate the floor structures, $S1$ and $S2$, concerning the vibration serviceability and impact sound insulation.

3.1 Vibration serviceability

A recent review on steel-timber composite floors [39] states AISC Design 11 [40] and CCIP-016 [41] as currently the most adequate references concerning vibrations of hybrid steel-timber systems. According to [41], the regulations described in the document apply to structures made of plenty of construction materials with walking excitation. For floor structures with natural frequencies above 4 Hz, the impulsive response calculation procedure is adopted as shown in Algorithm 3.1.

The response factor can be calculated utilizing the acceleration time history from Algorithm 3.1, which is related to continuous vibration. Nevertheless, a continuous vibration is seldom the case. Consequently, the concept of VDV proposed in [40] is used to estimate the acceptability of intermittent vibration:

$$VDV = \left(\int_0^T a^4(t)\text{dt}\right)^{1/4} = 0.68 a_{\text{w,rms}}(n_{\text{day/night}} T_{\text{single}})^{1/4} \quad (8)$$

with $a_{w,\text{rms}}$ the RMS-acceleration response from Algorithm 3.1, $n_{\text{day}} = 32$, $n_{\text{night}} = 16$ and the time it takes to cross the floor

$$T_{\text{single}} = \frac{d_{\text{floor}}}{v_{\text{step}}} = \frac{\sqrt{(l^2 + b^2)}}{(1.67 f_w^2 - 4.83 f_w + 4.50)}. \quad (9)$$

Consequently, FE modal analysis is adopted to identify the fundamental frequency f_1, the natural frequencies f_m of modes up to twice the fundamental frequency, and the corresponding modal masses $\hat{m}_m$ of these modes. The modal damping ratios are taken as 1%, as recommended by [36].

3.2 Impact sound

The standard ISO 10140-5 [23] specifies procedures to measure impact sound properties. Here, the tapping machine is described as excitation for impact sound measurements. A numerical version of the tapping machine is used in this work. The procedure to compute the loading that is applied to the FE model is described in the following.

Brunskog et al. [43] provide a method to calculate the discrete frequency spectrum of the impact loading due to a standard tapping machine. The floor is described by a general frequency-dependent driving-point impedance Z_{dp}. The hammer impact force $f_0(\text{t}) = F_0\delta(t)$ is applied to the structure. This yields the frequency-dependent force $f_0(\omega) = F_0$ by a Fourier transform which varies between $2M_0v_0$ and M_0v_0 for an elastic and plastic impact where $v_0 = 0.886$ m/s is the initial hammer velocity and $M_0 = 0.5$ kg equals the weight of a hammer. Here, the geometric mean $\sqrt{2}M_0v_0$ is considered [44]. The spectrum of the continuing impact is given as

$$f_1'(\omega) = \frac{f_0}{1 + i\omega M_0/Z_{\text{dp}}}. \quad (10)$$

Then, an inverse Fourier transform computes the corresponding force in time $f_1'(t)$. The time of the zero crossing $t_{\text{cut}} = \{\min t | t > 0, f_1'(t) = 0\}$ is found and the force spectrum $F_1(\omega)$ is computed by a Fourier transform. Finally the Fourier series components $F_n = F_1(nf_h)f_h$ with $f_h = 1/T_h$ and $T_h = 0.5$ s for each of the five hammers are applied to the floor structure at the respective frequencies [43]. An exemplary plot of the tapping machine load over frequency is given in Figure 10.

Furthermore, the driving-point impedance of the floor is computed from the local Z_{L} and global impedance Z_{G} as follows [38]:

$$Z_{\text{dp}} = \frac{Z_{\text{G}}(\omega)Z_{\text{L}}(\omega)}{Z_{\text{G}}(\omega) + Z_{\text{L}}(\omega)}. \quad (11)$$

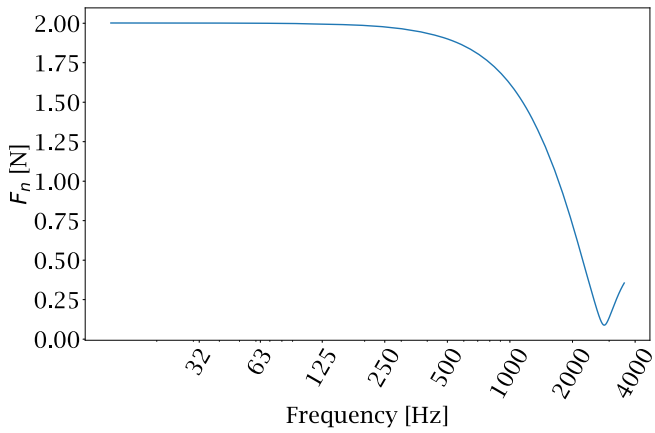

Figure 10. Example plot of load F_n against frequency.

The global impedance

$$Z_{\mathrm{G}}(\omega) = \frac{-iD_{jj}(\omega)}{\omega} \tag{12}$$

is found using the dynamic stiffness of the floor

$$D_{jj}(\omega) = -\omega^2 M_{jj} + K_{jj}(1 + ig) \tag{13}$$

taken from the FE model at the DOF j of the impact with M_{jj} and K_{jj} as mass and stiffness matrix entries and a material damping coefficient $g = 0.0084$ for the upper timber plate, which is derived from vibration measurements of the LVL plates.

The local impedance is analytically approximated [38]:

$$Z_L(\omega) = \frac{2Er_h}{i\omega(1+\nu)(1-\nu)}. \tag{14}$$

with r_h the hammer radius, the Poisson's ratio $\nu = \sqrt{\nu_{xy} \cdot \nu_{yx}}$, and the elasticity modulus $E = \sqrt{E_x \cdot E_y}$ of the respective material.

The computed force is used in the desired frequency range of f_{impact} as excitation on the structure in a time-harmonic analysis. The considered frequency range differs between open and closed cross- sections due to requirements concerning finite element sizes. Hence, $f_{\mathrm{impact},S1} \in [10, 1300]$ Hz and $f_{\mathrm{impact},S2} \in [10, 2400]$ Hz are applied as frequency ranges in the simulations. The resolution of $\Delta f = 2$ Hz for the impact sound calculations results from the repetition frequency of the hammers of the tapping machine. To determine impact sound characteristics, the sound power P is computed from the surface velocity of the lower surfaces of the samples, i.e., timber panels and radiating steel surfaces, using the Rayleigh integral [45, 46]. The sound power level is calculated from the computed sound power P as

$$L_{\mathrm{W}} = 10\log_{10}(P/10^{-12}). \tag{15}$$

Moreover, third-octave band data is calculated from the equidistant frequency data.

Since the goal is to compare normalized sound pressure levels for the hybrid steel- timber floors, sound power levels L_W are converted to sound pressure levels L_p according to the following relation from [47]:

$$L_p = L_W - \left\{10\log\left(\frac{A}{A_0}\right) + 4.34\frac{A}{S} + 10\log\left(1 + \frac{Sc}{8Vf}\right) + C_1 + C_2 - 6\right\} \tag{16}$$

where the equivalent absorption surface A of the room equals

$$A = \frac{55.26V}{cT_{60}}\ [\mathrm{m}^2]. \tag{17}$$

A reverberation time of $T_{60} = 0.45$ s is considered, as specified in [48] for the respective room volume $V = l \cdot b \cdot h_{\mathrm{room}} = 24.3\ \mathrm{m}^3$ where the room height is assigned to be $h_{\mathrm{room}} = 2.4$ m and length l and width b are taken from Table 1. Moreover, the reference surface $A_0 = 1\ \mathrm{m}^2$ and the sound wave velocity $c = 343$ m/s are specified. The overall surface of the room is computed as $S = l \cdot b \cdot h_{\mathrm{room}} \cdot 2 + b \cdot h_{\mathrm{room}} \cdot 2 = 51.1\ \mathrm{m}^2$. Furthermore, the center frequency of third-octaves f [Hz] and the correction terms

$$C_1 = -10\log\left(\frac{p_s}{p_{s,0}}\right) + 5\log\left[\frac{273.15+\theta}{\theta_0}\right], \tag{18}$$

as well as

$$C_2 = -10\log\left(\frac{p_s}{p_{s,0}}\right) + 15\log\left[\frac{273.15+\theta}{\theta_1}\right], \tag{19}$$

are required for equation (16). The calculation of the correction terms in equations (18) and (19) uses the static air pressure $p_s = 95$ kPa for an altitude of 500 m, the reference static air pressure $p_{s,0} = 101.325$ kPa, the air temperature $\theta = 293.2$ K (=20°), $\theta_0 = 314$ K and $\theta_1 = 296$ K. Subsequently, the following relation from [23] is applied

$$L_n = L_p + 10\log\left(\frac{A}{10\ \mathrm{m}^2}\right) \tag{20}$$

to compute the normalized impact sound pressure.

4 Results

In this section, the findings related to vibration serviceability and impact sound properties of the samples denoted as $S1$ and $S2$ are presented. The boundary conditions play a significant role in influencing the structural vibration and sound radiation in the low-frequency range. Unfortunately, measurements in a built-in situation have not been feasible. Thus, a comparative analysis is conducted between two extreme cases with different boundary conditions, namely, clamped ("c") and free ("f").

4.1 Vibration serviceability properties

The VDV is a critical metric for evaluating the potential for adverse comments in residential buildings, as prescribed

Table 5. VDV ranges for the probability of adverse comments

Place and time	Low probability [$ms^{-1.75}$]	Adverse comments possible [$ms^{-1.75}$]	Adverse comments probable [$ms^{-1.75}$]
Residential buildings day	0.2–0.4	0.4–0.8	0.8–1.6
Residential buildings night	0.1–0.2	0.2–0.4	0.4–0.8

Table 6. Fundamental frequencies $f_{1,j}$ [Hz], modes for the VDV evaluation $f_{m,j}$ [Hz], and modal masses $\hat{m}_{m,j}$ of the samples $j \in [S1,f; S1,c; S2,f; S2,c]$.

Sample j	$f_{1,j}$ [Hz]	$f_{m,j}$ [Hz]	$m_{m,j}$ [kg]
$S1,c$	49.81	{49.81; 56.82; 70.06; 89.54}	{0.28; 0.11; 0.04,0.03}
$S1,f$	17.75	{17.75; 22.45; 34.18}	{0.69; 0.34; 0.21}
$S2,c$	63.42	{63.42; 66.96; 74.34; 84.20; 88.19; 88.99; 90.23; 92.47; {92.50; 107.6; 108.73; 110.2; 112.73; 112.80; 116.78}	{1.93; 0.43; 0.18; 0.11; 0.10; 0.10; 0.07; 0.08; {0.09; 0.06; 0.05; 0.06; 0.06; 0.42; 0.14}
$S2,f$	5.29	{5.29}	{14.97}

by the British Standard BS 6472-1 [42]. The respective limit values for the VDV are given in Table 5, which are compared with the VDV calculated for all samples $j \in [S1,f; S1,c; S2,f; S2,c]$ using Algorithm 3.1 and equation (8). This computation involves determining fundamental frequencies $f_{1,j}$, modes to be considered $f_{m,j}$, and modal masses $\hat{m}_{m,j}$ through FE modeling. The results for the different sample configurations are presented in Table 6.

Upon evaluating the VDV for the test specimens, as shown in Table 7, several observations emerge. Firstly, it is evident that $S2,c$ exhibits a higher number of modes within the specified frequency range $\Delta f_{S2,c} \in [0, 2 \cdot f_{1,S2,c}]$, primarily due to its relatively high fundamental frequency $f_{1,S2,c}$ and the presence of numerous localized modes originating within the steel frame, which is not as pronounced in $S1$. Secondly, $S2,f$ has a relatively low fundamental natural frequency $f_{1,S2,f}$, necessitating consideration of only the fundamental mode within the observed range of $\Delta f_{S2,f} \in [0,2 \cdot f_{1,S2,f}] = [0, 10.58]$ Hz.

In terms of day and night VDV, samples $S1,c$, $S1,f$, and $S2,c$ exhibit similar values, around 0.57. Notably, $S2,f$ stands as an outlier, with a VDV reaching up to 1.67, indicating problematic vibrational behavior. The other samples fall within the "adverse comments possible" range, while $S2,f$ exceeds this threshold and falls into the category of "adverse comments probable". However, the behavior of a built-in floor structure, which presumably lies between the extreme boundary conditions of free and clamped, yields VDV values that also fall within a range between "possible" and "probable" adverse comments.

As specified in Algorithm 3.1, the structural response depends on the damping ratio, which has been fixed using normative specifications. Hence, uncertainty related to the damping remains and should be kept in mind when interpreting the results.

4.2 Impact sound properties

The results of impact sound pressure levels are examined from two perspectives: the influence of different boundary conditions, i.e., free "f" and clamped "c", and the effect of the two distinct cross-section types, i.e., open and closed. The comparison of the impact sound results under the different boundary conditions "f" and "c" is depicted in Figure 11.

Table 7. VDV during the day $VDV_{d,j}$ [$ms^{-1.75}$] and VDV during the night $VDV_{n,j}$ [$ms^{-1.75}$] of the samples $j \in [S1,f; S1,c; S2,f; S2,c]$.

Sample j	$VDV_{d,j}$ [$ms^{-1.75}$]	$VDV_{n,j}$ [$ms^{-1.75}$]
$S1,c$	0.65	0.55
$S1,f$	0.57	0.46
$S2,c$	0.57	0.48
$S2,f$	1.67	1.41

Two insights can be gained from these plots. Firstly, as anticipated, the impact of boundary conditions is most pronounced in the lower frequency range, up to 80 Hz for $S1$ and up to 500 Hz for $S2$. Secondly, the impact of boundary conditions is more substantial for the closed specimen $S1$ compared to the open one $S2$ up to 100 Hz. This discrepancy arises because, in the clamped case, all edges of the lower timber panel are fixed for $S1$, whereas for $S2$, only the edges at the longitudinal ends of the lower timber panel are fixed, resulting in a greater influence of boundary conditions in the low-frequency range for $S1$.

Furthermore, a comparison of the different cross-section types, open and closed, under both boundary conditions is presented in Figure 12.

Both cross-section types exhibit similar quantitative behavior, with $S1$ displaying slightly higher sound pressure levels in some third octaves, specifically about 5 dB higher than $S2$. This observation suggests that $S2$ radiates slightly less sound than $S1$. Qualitatively, the two configurations share similar curve shapes, but slight shifts in characteristics are observed in frequency due to their different structural setups. For instance, under clamped support conditions, both specimens initially exhibit a low sound pressure level at lower frequencies, at approximately

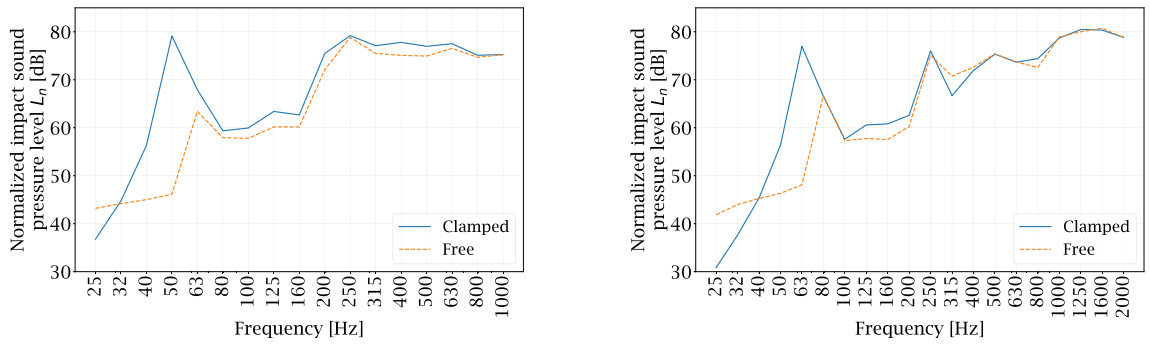

(a) (b)

Figure 11. Normalized impact sound pressure of samples $S1$ (a) and $S2$ (b) for the cases "f" and "c" for third-octave bands.

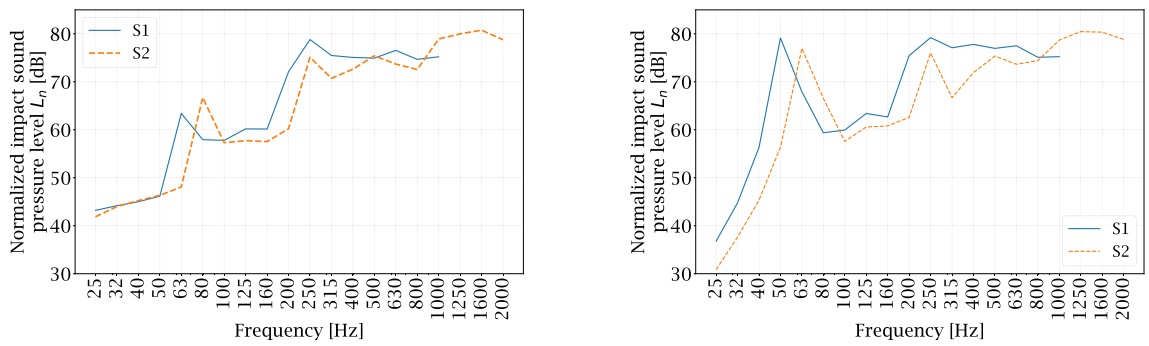

(a) (b)

Figure 12. Comparison of the sound pressure levels of the samples $S1$ (closed) and $S2$ (open) for the cases "f" (a) and "c" (b) for third-octave bands.

30 Hz. Subsequently, a distinct peak is shown at roughly 50 Hz for $S1$ and approximately 63 Hz for $S2$. Notably, the peak for $S2$ shifts to the adjacent third-octave band due to the resonant behavior of the structure. Furthermore, qualitative disparities become evident in the clamped support scenario within the frequency range of 160–800 Hz, where $S2$ demonstrates more fluctuations in sound pressure levels than $S1$.

To provide context for the impact sound behavior of the hybrid steel-timber floors, the impact sound pressure level values from Table B.2 of ISO 12354-2 [49] for concrete floors (100 mm and 180 mm thick) with a bonded screed layer (20 mm and 50 mm thick) are included for comparison in Figure 13. The lower and upper bounds of sound pressure levels for the hybrid steel-timber floors are established, offering a range of in-situ behavior. This means that in every third-octave band, the minimum value of the four sound pressure levels, i.e., $S1$,f, $S1$,c, $S2$,f and $S2$, c, is identified and taken as a value for the lower bound and vice versa for the upper bound.

In the low-frequency range up to 200 Hz, the lower and upper bounds cover values similar to those of concrete floors. In the mid-frequency range, up to around 1000 Hz, the hybrid floors' sound pressure levels fall between the two concrete floors. Beyond 1000 Hz, the hybrid floors exhibit sound pressure levels higher than the concrete floors,

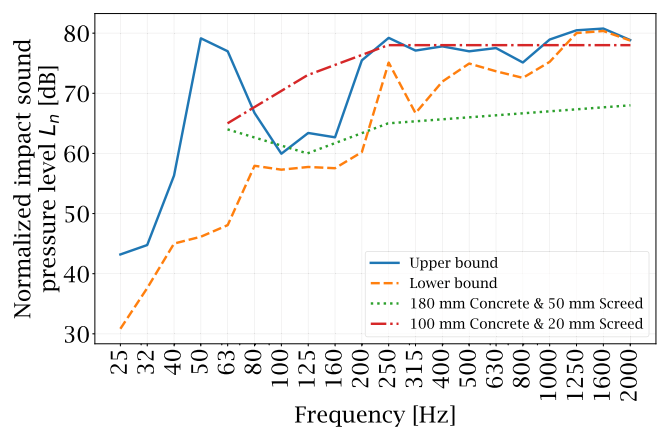

Figure 13. Comparison of the upper and lower bounds of the sound pressure levels computed for the hybrid floor samples $S1$ and $S2$ with the values for a 100 mm thick concrete floor with a 20 mm thick bonded screed and a 180 mm thick concrete floor with a 50 mm thick bonded screed provided in [40]. Results are given in third-octave bands for the upper and lower bounds and in octaves for the concrete floors.

with a decreasing trend at 2000 Hz. This indicates that the levels may approach those of concrete floors at higher frequencies. However, this could not be definitively verified

due to the limited computational resources and, hence, limited observed frequency ranges. Additionally, it should be noted that the damping and joint stiffness values are chosen based on assumptions explained in previous sections. Thus, the interpretation of the results is subject to the respective modeling choices. In conclusion, the hybrid floors demonstrate behavior similar to concrete floors. However, influences of additional structural components of a built-in situation, e.g., floating floors, are not considered in this study. Hence, a more realistic setting in a building might give more insight into the comparison of the floor types.

5 Discussion

In the present study, the FE models of the hybrid floor structures rely on parameters derived from the calibration of FE models of smaller specimens. It is worth noting that this step assumes the transferability of these parameters, a presumption that should be validated through future large-scale tests. Moreover, the construction of all models, both for small- and large-scale specimens, is based upon certain assumptions. These assumptions cover factors such as the appropriateness of the realization of free boundaries in the measurements and the suitability of the employed joint and structural model. The results indicate that the structural behavior has been reasonably approximated.

The assessment of vibration serviceability, as evaluated by the VDV, emphasizes concerns related to potential resident annoyance. Observably, none of the examined cases exhibit a low probability of adverse comments. One potential remedy for enhancing the performance of these floor structures involves increasing the distributed mass of the floor. However, such a mass increase necessitates accurate adjustment, as it concurrently affects the natural frequency of the floor – a factor of substantial significance for vibration serviceability as a too-low fundamental frequency may pose a challenge. Additionally, another potential strategy for mitigating the issue of high VDV involves increasing inherent damping. Investigating the damping characteristics in greater detail may provide valuable insights for effectively addressing this concern.

Regarding impact sound pressure levels, as expected, the influence of boundary conditions is most pronounced in the lower frequency range. Furthermore, the open and closed cross-sections display quite similar behavior, thus making the open setup only slightly more convenient for practical applications. When the performance of the hybrid structures is compared with commonly used concrete floors with bonded screed, it becomes evident that a similar level of performance can be achieved. Still, it is to be noted that a built-in situation in buildings differs from the tested setting as usually floating floors or soft coverings are applied to further reduce impact sound noise. This step is commonly performed after the floor installation for both concrete and hybrid steel-timber floors. Compared to the concrete floors, the hybrid floors might be considered beneficial in terms of weight and sustainability.

6 Conclusions

In conclusion, this investigation explores novel hybrid steel-timber floor elements, primarily focusing on their vibration serviceability and impact sound performance. Leveraging Finite Element analysis techniques, this study provides a comprehensive examination of the behavior of these innovative building components in terms of vibroacoustics. First, the Finite Element model is validated by aligning it with experimental data on natural frequencies and modes and determining joint stiffness values. This calibrated model serves as the basis for the in-depth analysis of vibration serviceability. This analysis expressed through vibration dose values, offers an initial insight into the real-world performance of these hybrid floor elements. Additionally, this study numerically explores the hybrid steel-timber floors' impact sound insulation properties, an aspect that has received limited attention in previous research. The outcomes presented herein reveal that the proposed building elements exhibit comparable behavior to that of conventional concrete ceilings, thus making the application of hybrid steel-timber floors feasible for future construction projects. The assumptions related to the structural damping and the applicability of the joint stiffness parameters at higher frequencies must be kept in mind, and further investigations in this regard are still required. Moreover, analyses in a realistic setting utilizing additional structural components, e.g., floating floors, will lead to more detailed insights into the impact sound insulation. It is worth noting that while the resultant vibration amplitudes, as quantified by vibration dose values, mostly fall within the range of possible adverse comments, there remain possibilities to further investigate the damping behavior of large-scale floor structures, which might support their broader adoption in construction practices. Laboratory tests on large-scale floor structures might further be used to validate the impact force applied to the FE model using an ISO tapping machine.

Acknowledgments

The authors gratefully acknowledge the help of the chair of *Timber Structures and Building Construction* at *Karlsruhe Institute of Technology* for assistance with the measurements. Furthermore, the authors are thankful for the support of the manufacturers in providing the materials for the samples. The authors thank Semere Gebrekidan for the valuable comments and corrections that helped to improve the manuscript.

Funding

This study was financially supported by the German Federal Ministry of Food and Agriculture through the Fachagentur Nachwachsende Rohstoffe e.V. (FNR) (grant number 22009817) and the German Research Foundation (DFG) (grant number MA2395/15-2).

Conflict of interest

Author declared no conflict of interests.

Data availability statement

Data are available on request from the authors.

Author contribution statement

Bettina Chocholaty: Conceptualization, Methodology, Software, Data Curation, Validation, Formal Analysis, Visualization, Writing – original draft, Writing – review & editing. *Nicolaas Bernardus Roozen*: Conceptualization, Methodology, Writing – review, Supervision. *Karl-Alexander Hoppe*: Methodology, Writing - review & editing. *Marcus Maeder*: Writing – review, Supervision. *Steffen Marburg*: Funding acquisition, Resources, Supervision, Writing – review.

References

1. A. Chiniforush, M.M. Alamdari, U. Dackermann, H. Valipour, A. Akbarnezhad: Vibration behaviour of steel-timber composite floors, part (1): experimental & numerical investigation. Journal of Constructional Steel Research 161 (2019) 244–257.
2. A. Hassanieh, A.A. Chiniforush, H.R. Valipour, M.A. Bradford: Vibration behaviour of steel-timber composite floors, part (2): evaluation of human-induced vibrations. Journal of Constructional Steel Research 158 (2019) 156–170.
3. M. Fujita, J. Sakai, H. Oda, M. Iwata: Building system for a composite steel-timber structure. Steel Construction 7 (2014) 183–187.
4. A.T. Balasbaneh, W. Sher, D. Yeoh, K. Koushfar: LCA & LCC analysis of hybrid glued laminated timber–concrete composite floor slab system. Journal of Building Engineering 49 (2022) 104005.
5. W. Zhu, H. Yang, W. Liu, B. Shi, Z. Ling, H. Tao: Experimental investigation on innovative connections for timber–concrete composite systems. Construction and Building Materials 207 (2019) 345–356.
6. A. Hassanieh, H. Valipour, M. Bradford: Experimental and numerical study of steel-timber composite (STC) beams. Journal of Constructional Steel Research 122 (2016) 367–378.
7. J. Negreira, A. Trollé, K. Jarnerö, L.-G. Sjökvist, D. Bard: Psychovibratory evaluation of timber floors – towards the determination of design indicators of vibration acceptability and vibration annoyance. Journal of Sound and Vibration 340 (2015) 383–408.
8. J. Weckendorf, G. Hafeez, G. Doudak, I. Smith: Floor vibration serviceability problems in wood light-frame buildings. Journal of Performance of Constructed Facilities 28 (2014) A4014003.
9. A. Pavic: Results of IStructE 2015 survey of practitioners on vibration serviceability. In: Proceedings of the SECED 2019 Conference: Earthquake Risk and Engineering towards a Resilient Word, London, UK, 9–10 September, 2019.
10. O.A. Hassan, F. Öberg, E. Gezelius: Cross-laminated timber flooring and concrete slab flooring: a comparative study of structural design, economic and environmental consequences. Journal of Building Engineering 26 (2019) 100881.
11. N. Perković, V. Rajčić, J. Barbalić: Analytical and numerical verification of vibration design in timber concrete composite floors, Forests 12 (2021) 707.
12. N.-G. Vardaxis, D. Bard Hagberg, J. Dahlström: Evaluating laboratory measurements for sound insulation of cross-laminated timber (CLT) floors: configurations in lightweight buildings. Applied Sciences 12 (2022) 7642.
13. F.G. Branco, L. Godinho: On the use of lightweight mortars for the minimization of impact sound transmission. Construction and Building Materials 45 (2013) 184–191.
14. L. Godinho, R. Masgalos, A. Pereira, F. Branco: On the use of a small-sized acoustic chamber for the analysis of impact sound reduction by floor coverings. Noise Control Engineering Journal 58 (2010) 658–668.
15. Technical Committee ISO/TC 98: ISO 10137 – Bases for design of structures – Serviceability of buildings and walkways against vibrations, International Organization for Standardization, Geneva, Switzerland, 2007.
16. B. Szabó, I. Babuška: Finite Element Analysis: Method, Verification and Validation. John Wiley & Sons, 2021.
17. J.E. Mottershead, M. Link, M.I. Friswell, C. Schedlinski: Model Updating. In: R. Allemang, P. Avitabile, Eds. Handbook of experimental structural dynamics. Springer, New York, NY, 2021, pp. 1–53.
18. B. Shahriari, K. Swersky, Z. Wang, R.P. Adams, N. De Freitas: Taking the human out of the loop: A review of bayesian optimization. Proceedings of the IEEE 104 (2015) 148–175.
19. S. Tao, A. Van Beek, D.W. Apley, W. Chen: Multi-model bayesian optimization for simulation-based design. Journal of Mechanical Design 143 (2021) 111701.
20. D. Owolabi, C. Loss, J. Zhou: Vibration properties and serviceability performance of a modular cross-laminated timber-steel composite floor system. Journal of Structural Engineering 149 (2023) 04023171.
21. B. Chocholaty, N.B. Roozen, M. Maeder, S. Marburg: Vibroacoustic response of steel–timber composite elements. Engineering Structures 271 (2022) 114911.
22. F. Nogueira: Bayesian Optimization: Open source constrained global optimization tool for Python, 2014. Available at https://github.com/fmfn/BayesianOptimization.
23. Technical Committee ISO/TC 43: DIN EN ISO 10140–5 – Acoustics – Laboratory measurement of sound insulation of building elements – Part 5: Requirements for test facilities and equipment, European Committee for Standardization, Brussels, Belgium, 2021.
24. Pollmeier Massivholz GmbH & Co.KG: Leistungserklärung einer Platte in Baubuche.2018. Available at https://www.pollmeier.com/de/produkte/ueber-baubuche/baubuche-platte (accessed: 2022-01-19).
25. A. Andrej: Schneider: Bautabellen für Ingenieure, vol. 21. Bundesanzeiger Verlag, 2014.
26. ANSYS, Inc.: Ansys engineering simulation software, 2019. Available at https://www.ansys.com/.
27. P. Langer, M. Maeder, C. Guist, M. Krause, S. Marburg: More than six elements per wavelength: The practical use of structural finite element models and their accuracy in comparison with experimental results. Journal of Computational Acoustics 25 (2017) 1750025.
28. L. Cremer, M. Heckl: Abstrahlung von Körperschall. In: L. Cremer, M. Heckl, Körperschall. Springer, 1996, pp. 459–545. https://doi.org/10.1007/978-3-662-08182-2.
29. D.J. Ewins: Modal testing – theory, practice and application. John Wiley & Sons, New York, 2009.
30. S. Ereiz, I. Duvnjak, J.F. Jiménez-Alonso: Review of finite element model updating methods for structural applications. Structures 41 (2022) 684–723.
31. R.J. Allemang: The modal assurance criterion – twenty years of use and abuse. Sound and vibration 37 (2003) 14–23.
32. O. Cuate, O. Schütze: Pareto explorer for finding the knee for many objective optimization problems. Mathematics 8 (2020) 1651.
33. K. Christodoulou, E. Ntotsios, C. Papadimitriou, P. Panetsos: Structural model updating and prediction variability using pareto optimal models. Computer Methods in Applied Mechanics and Engineering 198 (2008) 138–149.
34. E. Brochu, V.M. Cora, N. De Freitas: A tutorial on bayesian optimization of expensive cost functions, with application to active user modeling and hierarchical reinforcement learning. 2010. Preprint available at https://arxiv.org/abs/1012.2599.
35. C.Q. Howard, B.S. Cazzolato: Acoustic Analyses using MATLAB® and ANSYS®. CRC Press, 2014.
36. Technical Committee CEN/TC 250: DIN EN 1995 1–1 – Eurocode 5: Design of timber structures, Part 1–1: General – Common rules and rules for buildings, European Committee for Standardization, Brussels, Belgium, 2010.
37. C. Geweth, S. Baydoun, F. Saati, K. Sepahvand, S. Marburg: Effect of boundary conditions in the experimental determination of structural damping. Mechanical Systems and Signal Processing 146 (2021) 107052.
38. P. Wang, C. Van Hoorickx, G. Lombaert, E. Reynders: Numerical prediction and experimental validation of impact sound radiation by timber joist floors. Applied Acoustics 162 (2020) 107182.
39. N. Cheraghi-Shirazi, K. Crews, S. Malek: Review of vibration assessment methods for steel-timber composite floors. Buildings 12 (2022) 2061.
40. T. Murray, D. Allen, E. Ungar, D. Davis: Vibrations of steel-framed structural systems due to human activity: AISC design guide 11. American Institute of Steel Construction, USA, 2016.
41. M.R. Willford, P. Young: A design guide for footfall induced vibration of structures. Concrete Society for the Concrete Centre London, London, UK, 2006.
42. Committee GME/21: BS 6472–1 – Guide to evaluation of human exposure to vibration in buildings – part 1: vibration sources other than blasting, 2008. https://doi.org/10.3403/19971044U.

43. J. Brunskog, P. Hammer: The interaction between the ISO tapping machine and lightweight floors. Acta Acustica united with Acustica 89 (2003) 296–308.
44. J. Lietzén, J. Miettinen, M. Kylliäinen, S. Pajunen: Impact force excitation generated by an ISO tapping machine on wooden floors. Applied Acoustics 175 (2021) 107821.
45. D. Fritze, S. Marburg, H.-J. Hardtke: Estimation of radiated sound power: a case study on common approximation methods. Acta Acustica united with Acustica 95 (2009) 833–842.
46. F. Fahy: Sound and structural vibration: radiation, transmission and response, Academic Press, London and Orlando, FL, 1985.
47. Technical Committee CEN/TC 211: DIN EN ISO 3741 – Acoustics – determination of sound power levels and sound energy levels of noise sources using sound pressure – Precision methods for reverberation test rooms, 2011. https://doi.org/10.31030/1642422.
48. Subcommittee NA 001-02-03-03 UA: DIN 18041 – Acoustic quality in rooms – Specifications and instructions for the room acoustic design, 2016. https://doi.org/10.31030/2395845.
49. Technical Committee CEN/TC 126: DIN EN ISO 12354-2 – Building acoustics – estimation of acoustic performance of buildings from the performance of elements – part 2: impact sound insulation between rooms, 2017. https: //doi.org/10.31030/2625099.

Cite this article as: Chocholaty B. Roozen NB. Hoppe K-A. Maeder M. & Marburg S. 2024. Vibration and impact sound properties of hybrid steel-timber floor structures. Acta Acustica, **8**, 11.